Simulation of Nitroxide Electron Paramagnetic Resonance Spectra from Brownian Trajectories and Molecular Dynamics Simulations

Susan C. DeSensi,* David P. Rangel,† Albert H. Beth,‡ Terry P. Lybrand,* and Eric J. Hustedt‡
*Department of Chemistry and Center for Structural Biology, Vanderbilt University, Nashville, Tennessee 37235; †Department of Chemistry, University of Washington, Seattle, Washington 98195; and ‡Department of Molecular Physiology and Biophysics, Vanderbilt University, Nashville, Tennessee 37232

ABSTRACT A simulated continuous wave electron paramagnetic resonance spectrum of a nitroxide spin label can be obtained from the Fourier transform of a free induction decay. It has been previously shown that the free induction decay can be calculated by solving the time-dependent stochastic Liouville equation for a set of Brownian trajectories defining the rotational dynamics of the label. In this work, a quaternion-based Monte Carlo algorithm has been developed to generate Brownian trajectories describing the global rotational diffusion of a spin-labeled protein. Also, molecular dynamics simulations of two spin-labeled mutants of T4 lysozyme, T4L F153R1, and T4L K65R1 have been used to generate trajectories describing the internal dynamics of the protein and the local dynamics of the spin-label side chain. Trajectories from the molecular dynamics simulations combined with trajectories describing the global rotational diffusion of the protein are used to account for all of the dynamics of a spin-labeled protein. Spectra calculated from these combined trajectories correspond well to the experimental spectra for the buried site T4L F153R1 and the helix surface site T4L K65R1. This work provides a framework to further explore the modeling of the dynamics of the spin-label side chain in the wide variety of labeling environments encountered in site-directed spin labeling studies.

INTRODUCTION

Site-directed spin labeling (SDSL) is a powerful technique for studying protein structure and dynamics. In SDSL studies, a spin label (e.g., methanethiosulfonate spin label; MTSSL) is introduced at a specific position in a protein and electron paramagnetic resonance (EPR) spectroscopy is used to measure physical characteristics at that position, including the mobility of the spin label side chain, the accessibility of the label to paramagnetic relaxation agents, and the distance between pairs of spin labels (for reviews, see (1–7)). Single spin label measurements at sequential positions in a protein reveal patterns of probe mobility and solvent accessibility that are indicative of secondary and tertiary structure. Internitroxide distance measurements can be utilized to orient these structural elements with respect to each other.

Interpreting SDSL results in terms of protein structure and dynamics is complicated by the length and flexibility of the MTSSL side chain (Fig. 1 *A*). The MTSSL tether has five torsion angles (χ_1 through χ_5) about which it can rotate independently of the protein backbone. Depending on these torsion angles, the unpaired electron that is localized to the nitroxide bond is ~7 Å from the C_α atom of the protein backbone. Detailed, context-specific knowledge of the orientation and dynamics of the MTSSL side chain will lead to a better understanding of how both side-chain dynamics and backbone dynamics combine to determine the EPR lineshape, how interelectron distances measured by EPR relate to C_α-C_α distances, and whether distributions of interelectron distances are due to distributions of side-chain conformations or distributions of backbone structures.

A variety of computational approaches have been used to model the orientation and dynamics of MTSSL and other spin-label side chains (e.g., (8–18)). Fajer and co-workers have developed a Monte Carlo approach for estimating the mobility and orientation of spin labels in known protein structures (12) and have subsequently applied this same method to estimate electron-electron distances between pairs of spin labels (14). Budil and co-workers (17) used short molecular dynamics (MD) simulations to characterize the local motion of MTSSL at two sites in T4 lysozyme (T4L). Ordering potentials were obtained from analysis of these MD simulations and spectra were then calculated for these potentials from steady-state solutions to the stochastic Liouville equation (SLE). Steinhoff and co-workers have also used MD simulations to derive single particle potentials describing the local motions of MTSSL in a polyleucine α-helix trimer (8) and for a consecutive series of sites in bacteriorhodpsin (16). Brownian dynamics trajectories for spin labels were generated from these single particle potentials and then used to calculate free induction decays (FID) and the corresponding continuous wave (CW)-EPR spectra using an approach originally developed by Robinson and co-workers (19). The calculation of FIDs from trajectories has been used to compute EPR spectra directly from Monte Carlo dynamics simulations of spin-labeled fatty acids in lipid bilayers (20) and from MD simulations of spin-labeled dipalmitoylphosphatidylcholine in dipalmitoylphosphatidylcholine bilayers

Submitted November 7, 2007, and accepted for publication December 27, 2007.

Address reprint requests to Eric J. Hustedt, 735B Light Hall, Vanderbilt University, Nashville, TN 37232. Tel.: 615-322-3181; Fax: 615-322-7236; E-mail: eric.hustedt@vanderbilt.edu.

Susan C. DeSensi's present address is Dept. of Chemistry, Boston University, Boston, MA 02215.

Editor: Betty J. Gaffney.

0006-3495/08/05/3798/12 $2.00

doi: 10.1529/biophysj.107.125419

(21). Stoica has used this same approach to calculate high-field EPR spectra from MD simulations of two spin-labeled mutants of T4L (13). Due to the brief duration of the MD simulations performed and other sampling issues, these calculated spectra were of insufficient quality to compare to experimental data.

The calculation of CW-EPR spectra directly from MD trajectories of spin-labeled proteins without any additional parameterization of the local dynamics and the comparison of those calculated spectra with experimental data would constitute a highly sensitive test of how well the behavior of the labeled protein in silico corresponds to its actual behavior in vitro. The approach used here builds upon the previous work cited above while overcoming the sampling issues encountered by Stoica. One distinct advantage of this approach is that no additional parameterization of the local dynamics is required. MD simulations are used to define both the amplitudes and rates of the local motions experienced by the spin label.

At X-band, CW-EPR spectra of spin-labeled proteins depend on the local dynamics of the spin label, internal motions of the protein, and the global rotational diffusion (GRD) of the protein. To account for GRD, a quaternion-based Monte Carlo method is developed to generate Brownian trajectories for an arbitrary GRD tensor. To account for all local and internal motions, multiple trajectories are extracted from a MD simulation of the spin-labeled protein. Trajectories for GRD and for local dynamics are combined to generate a set of trajectories defining the total rotational dynamics of the spin label as a function of time. From this set of trajectories, FIDs are calculated by simulating the spin dynamics of the electron after a $\pi/2$ pulse using the SLE. An ensemble-averaged FID is then calculated and the CW-EPR spectrum is obtained by Fourier transform. The details of these procedures are given in Methods.

In the Results section, it is first established that trajectories on the order of 50–100 ns are required to use this approach to simulate the X-band CW-EPR spectrum of a nitroxide spin label. Simulations of the CW-EPR spectra from time-domain Brownian trajectories of a nitroxide spin label undergoing GRD are shown to be identical to those obtained by an eigenfunction expansion approach to finding the steady-state solution to the SLE (22,23). MD simulations are then performed for T4L spin labeled at two sites chosen to represent distinctly different labeling topologies. Designating the MTSSL-labeled cysteine residue as **R1,** T4L F153R1 is a buried site whereas T4L K65R1 is a solvent-exposed helix surface site (Fig. 1 *B*). The behavior of the MTSSL side chains during these MD simulations is consistent with expectations for buried and solvent-exposed sites, respectively. CW-EPR spectra at these two sites are calculated considering the combined effects of GRD and internal dynamics. The resulting calculated spectra correspond reasonably well to experimental data.

Portions of this work have been previously published as an Abstract (24).

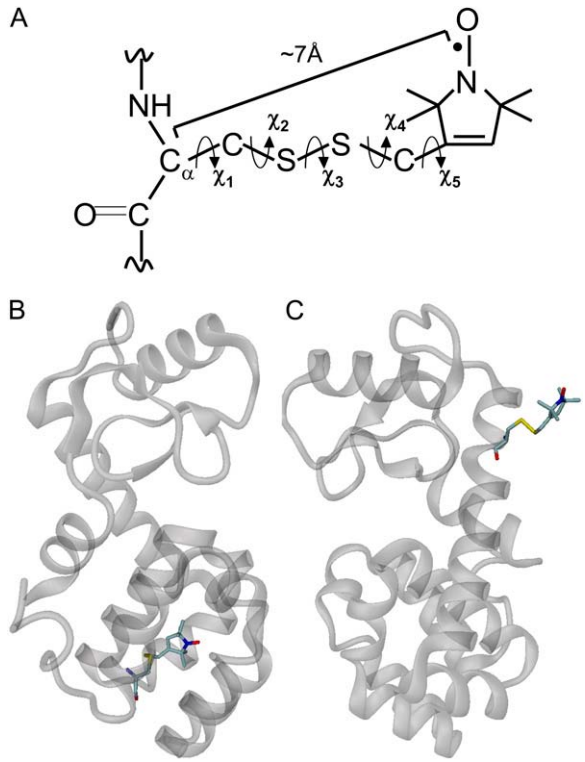

FIGURE 1 (*A*) Structure of a MTSSL-labeled cysteine residue (**R1**) showing the five torsion angles between C_α and the nitroxide ring. Depending on these torsion angles, the distance from C_α to the unpaired electron localized to the N-O bond is ~7 Å. (*B*) Crystal structure of T4L (37) with a spin-labeled cysteine substituted at residue 153. (*C*) Crystal structure of T4L with a spin-labeled cysteine substituted at residue 65.

METHODS

Generation of GRD trajectories

The calculation of the CW-EPR spectrum for a nitroxide undergoing GRD requires the generation of an appropriate set of Brownian trajectories. These trajectories will give the rotation matrix, $\hat{R}_{\mathrm{GRD}}(t)$, that defines the orientation of the protein rotational diffusion tensor in the laboratory frame as a function of time. A Monte Carlo method that uses quaternions (25,26) to represent rotations is employed to generate these trajectories. A similar algorithm has previously been developed by Fedchenia et al. (27). Using the Euler angle convention of Edmonds (28), the quaternions are defined in terms of the Euler angles according to Eq.1:

$$\vec{q}(t) = \begin{pmatrix} q_0(t) \\ q_1(t) \\ q_2(t) \\ q_3(t) \end{pmatrix} = \begin{pmatrix} \cos\dfrac{\theta(t)}{2}\cos\dfrac{(\phi(t)+\psi(t))}{2} \\ \sin\dfrac{\theta(t)}{2}\sin\dfrac{(\phi(t)-\psi(t))}{2} \\ -\sin\dfrac{\theta(t)}{2}\cos\dfrac{(\phi(t)-\psi(t))}{2} \\ -\cos\dfrac{\theta(t)}{2}\sin\dfrac{(\phi(t)+\psi(t))}{2} \end{pmatrix}. \quad (1)$$

The angular velocities about the x, y, and z axes are related to the time-derivatives of the three Euler angles by Eq. 2 (28):

$$\begin{pmatrix} \omega_x \\ \omega_y \\ \omega_z \end{pmatrix} = \begin{pmatrix} \sin\psi & -\sin\theta\cos\psi & 0 \\ \cos\psi & \sin\theta\sin\psi & 0 \\ 0 & \cos\theta & 1 \end{pmatrix} \begin{pmatrix} \dot{\theta} \\ \dot{\phi} \\ \dot{\psi} \end{pmatrix}. \quad (2)$$

Equation 2 can be rearranged to give the time-derivatives of the three Euler angles in terms of the angular velocities and the result substituted in to the time-derivative of Eq. 1 to give the time-dependent behavior of the quaternions:

$$\frac{d\vec{q}(t)}{dt} = \frac{1}{2}\begin{pmatrix} 0 & +\omega_x & +\omega_y & +\omega_z \\ -\omega_x & 0 & +\omega_z & -\omega_y \\ -\omega_y & -\omega_z & 0 & +\omega_x \\ -\omega_z & +\omega_y & -\omega_x & 0 \end{pmatrix}\vec{q}(t) = \frac{1}{2}\hat{M}\vec{q}(t). \tag{3}$$

The solution to Eq. 3 is given by

$$\vec{q}(t+\tau) = e^{\frac{1}{2}\hat{M}\tau}\vec{q}(t). \tag{4}$$

Noting that

$$\hat{M}\hat{M} = -(\omega_x^2 + \omega_y^2 + \omega_z^2)\hat{1}, \tag{5}$$

the exponential term in Eq. 4 can be written as

$$e^{\frac{1}{2}\hat{M}\tau} = \cos\left(\frac{\tau\sigma}{2}\right)\hat{1} + \frac{1}{\tau\sigma}\sin\left(\frac{\tau\sigma}{2}\right)\hat{M}\tau, \tag{6}$$

where

$$(\tau\sigma)^2 = (\delta_x)^2 + (\delta_y)^2 + (\delta_z)^2, \tag{7}$$

and

$$\vec{\delta} = \tau\vec{\omega}. \tag{8}$$

The angular displacements (δ_x, δ_y, and δ_z) about the x, y, and z axes are chosen at each time step using three random uniform deviates (r):

$$\delta_i = \varepsilon_i(2r-1) \quad i = x, y, z. \tag{9}$$

Following Schurr and co-workers (29), the appropriate values of ε_i can be determined by noting that in time $t = N\tau$ the total angular displacement, Δ_i, about axis i

$$\Delta_i = \sum_{k=1}^{N}(\delta_i)_k \tag{10}$$

should behave statistically such that

$$\langle\Delta_i^2\rangle = 2D_i t = 2D_i N\tau \tag{11}$$

for Brownian rotational diffusion. Since

$$\langle\Delta_i^2\rangle = N\langle\delta_i^2\rangle \tag{12}$$

and the δ_i are uniformly distributed on the interval $-\varepsilon_i \le \delta_i \le \varepsilon_i$ so that

$$\langle\delta_i^2\rangle = \frac{\varepsilon_i^2}{3}. \tag{13}$$

Then

$$\varepsilon_i = \sqrt{6D_i\tau}. \tag{14}$$

A given trajectory for GRD is generated by first selecting random initial values of the angles $\Omega_{GRD}(t=0)$ with the appropriate $\sin\theta$-weighting factor. The quaternion, $\vec{q}(t=0)$, is then calculated from Eq. 1. Angular displacements are then randomly selected according to Eqs. 9 and 14. The quaternion, $\vec{q}(t=\tau)$, is then calculated from

$$\vec{q}(t=\tau) = \left(\cos\left(\frac{\tau\sigma}{2}\right)\hat{1} + \frac{1}{\tau\sigma}\sin\left(\frac{\tau\sigma}{2}\right)\hat{M}\tau\right)\vec{q}(t=0), \tag{15}$$

and the rotation matrix is given by Eq. 16:

$$\begin{aligned}\hat{R}_{GRD}(t=\tau) &= \begin{pmatrix} q_0^2+q_1^2-q_2^2-q_3^2 & -2(q_0q_3-q_1q_2) & 2(q_0q_2+q_1q_3) \\ 2(q_0q_3+q_1q_2) & q_0^2-q_1^2+q_2^2-q_3^2 & -2(q_0q_1-q_2q_3) \\ -2(q_0q_2-q_1q_3) & 2(q_0q_1+q_2q_3) & q_0^2-q_1^2-q_2^2+q_3^2 \end{pmatrix} \\ &= \hat{R}_z(\psi)\hat{R}_y(\theta)\hat{R}_z(\phi) \\ &= \begin{pmatrix} \cos\psi & \sin\psi & 0 \\ -\sin\psi & \cos\psi & 0 \\ 0 & 0 & 1 \end{pmatrix}\begin{pmatrix} \cos\theta & 0 & -\sin\theta \\ 0 & 1 & 0 \\ \sin\theta & 0 & \cos\theta \end{pmatrix}\begin{pmatrix} \cos\phi & \sin\phi & 0 \\ -\sin\phi & \cos\phi & 0 \\ 0 & 0 & 1 \end{pmatrix}. \end{aligned} \tag{16}$$

The rotation matrix at additional time points is calculated by selecting new, random angular displacements and then calculating the resulting quaternion.

Parameterization of the MTSSL side chain

Force-field parameters for four new atom types (the unsaturated carbon atoms of the nitroxide ring, the saturated carbon atoms of the nitroxide ring, the nitroxide nitrogen, and the nitroxide oxygen) were derived from a gas-phase geometry optimization of a MTSSL-modified cysteine implemented in Gaussian 98 (30) with an unrestricted Hartree-Fock wave function and a 6-31G* basis set. Equilibrium bond lengths and angles were taken directly from this minimum energy structure and compared to the nitroxide spin label x-ray crystallography data of Lajzerwicz-Bonneteau (31) for validation. Force constants were interpolated using reference values in the AMBER99 force field (32,33) and the quantum mechanical calculations of Barone and co-workers (34). Torsional parameters for the new atom types were defined by analogy to preexisting atom types in the AMBER99 force field. The electrostatic potential of the geometry optimized MTSSL structure was then computed in Gaussian 98 using a 6-31G* basis set. The restrained electrostatic potential (35) module of the AMBER 8.0 suite of programs (36) was used to calculate atom-centered partial charges that reproduced the quantum mechanical electrostatic potential results.

MD simulations

The crystal structure of T4L (Protein Data Bank entry 3LZM (37)) was used as the starting structure for the MD simulations. The molecular graphics program PSSHOW (38) was used to construct the initial spin-labeled models of T4L. The phenylalanine at position 153 of T4L was replaced with the **R1** residue yielding the T4L F153R1 mutant. In a separate model, the lysine at position 65 was replaced with **R1** to create the T4L K65R1 mutant. Acetyl N-terminal residues and *N*-methyl C-terminal residues were added to the termini of both spin-labeled mutants.

MD simulations of T4L F153R1 and T4L K65R1 were performed with the AMBER 8.0 suite of programs together with the all-atom AMBER99

force field (32,33,35,36). Using the LEaP module of AMBER, the missing crystallographic hydrogens were added to the starting structures. Each of the resulting structures was placed in a truncated octahedron periodic box of SPC/E water molecules with a minimum 11 Å distance from the closest atom of the solute to any box edge. To maintain electroneutrality (39), seven and eight chloride counterions were added to the solvated structures of T4L F153R1 and T4L K65R1, respectively.

The SANDER module of AMBER was used to relax the solvated system with a series of steepest decent energy minimizations. First, positional restraints were imposed on the water molecules and counterions while the protein molecule was relaxed for 300 cycles of minimization. The water molecules and counterions were then energy minimized with 1000 cycles. Finally, 300 cycles of minimization were applied to the entire solvated system.

After minimization, a 20 ps constant volume MD simulation was performed to gradually heat the system to room temperature (298 K) and to allow the solute-water interface to relax. The water molecules and counterions were allowed to move freely, whereas the solute was restrained to prevent deviation from the initial coordinates. The system was then subjected to a series of short (0.2 ps), constant pressure MD simulations with different velocity assignments to uniformly distribute atomic velocities and equalize the temperature throughout the system (thermalization).

A 75 ns, production simulation (after minimization and equilibration) was run for both T4L F153R1 and T4L K65R1 at a temperature of 298 K maintained using a Langevin temperature piston under constant pressure conditions. The SHAKE algorithm was applied to maintain rigid bond lengths for bonds containing hydrogen atoms, and the particle mesh Ewald (PME) method was used to treat long-range electrostatic interactions (40,41). A 9 Å direct space, nonbonded cutoff and a 2 fs integration time step were used. Atomic coordinates were saved every 100 integration steps. The translational and rotational center-of-mass motion were removed every 200 steps.

Although the AMBER99 force field has typically been used with the TIP3P water potential, the TIP3P water model is not appropriate for use with long-range electrostatic correction methods such as PME (42). By contrast, the SPC/E water potential does retain good bulk water behavior when used with PME methods (43). It has been previously shown that the SPC/E water model in combination with the AMBER99 protein potential reproduces crystallographic water positions better than the TIP3P potential, suggesting that this protein/water potential pair is reasonable for equilibrium structural calculations in long MD simulations (44).

Extracting trajectories from MD simulation

The coordinates of the spin label are used to define the vectors corresponding to the X, Y, and Z axes of the nitroxide A- and g-tensors. These vectors are used to calculate the Euler angles, Ω_{MD}, which define the orientation of the nitroxide in the protein frame of reference. Since the global translational and rotational motions of the spin-labeled proteins are removed during the MD simulation, the protein frame of reference is fixed at an arbitrary orientation with respect to the laboratory reference frame. Translating the nitroxide nitrogen to the origin of the coordinate system, $\vec{O}$ is defined to be the coordinates of the nitroxide oxygen and the vectors $\vec{C}_3$ and $\vec{C}_7$ are defined to be the coordinates of the two carbon atoms bonded to the nitroxide nitrogen. The X axis of the nitroxide coordinate system is then given by

$$\vec{X} = \frac{\vec{O}}{|\vec{O}|}, \tag{17}$$

the Z axis by

$$\vec{Z} = \frac{\vec{C}_3 \times \vec{O} + \vec{O} \times \vec{C}_7}{|\vec{C}_3 \times \vec{O} + \vec{O} \times \vec{C}_7|}, \tag{18}$$

and the Y axis by

$$\vec{Y} = \vec{Z} \times \vec{X}. \tag{19}$$

The required Euler angles are given by

$$\theta_{MD} = \arccos(Z_z)$$
$$\phi_{MD} = \arctan\left(\frac{Y_z}{X_z}\right)$$
$$\psi_{MD} = \arctan\left(\frac{-Z_y}{Z_x}\right). \tag{20}$$

A Perl program was written to extract the necessary coordinate information from the MD simulation and calculate the Euler angles. The result is a set of Euler angles defining the orientation of the nitroxide with respect to the protein every 200 fs. This is a much smaller time increment than is required for calculation of the FID. As a result, multiple trajectories can be extracted from a single MD simulation with alternating direction of time as illustrated in Fig. 2. From a single MD simulation consisting of N_{MD} points, N_t trajectories are extracted each with N_c points ($N_c \times N_t = N_{MD}$).

Combining GRD and MD

To combine GRD with the internal and local motions as determined by MD, the total rotation is determined by

$$\hat{R}(\Omega(t)) = \hat{R}_{GRD}(t)\hat{R}_{PTD}\hat{R}_{MD}(\Omega_{MD}(t)), \tag{21}$$

where Ω_{MD} are the Euler angles determining the orientation of the spin label in the frame of the protein, $\hat{R}_{PTD}$ determines the orientation of that protein frame with respect to the rotational diffusion tensor of the protein, and $\hat{R}_{GRD}$ defines the orientation of the protein diffusion tensor in the laboratory frame. The rotation operator, $\hat{R}_{GRD}$, is defined in Eq. 16; $\hat{R}_{MD}$ is similarly defined using the angles in Eq. 20. In the special cases where either the rotational diffusion tensor is isotropic or there are no internal and local motions ($\hat{R}_{MD} = \hat{1}$), then the diffusion tensor frame can be ignored ($\hat{R}_{PTD} = \hat{1}$).

Calculation of FID

The spin Hamiltonian in the rotating frame is given by

$$\mathrm{H}(t) = (g_{zz}\beta_e H_0 - \omega_0)\hat{S}_z + \gamma_e A_{xz}\hat{I}_x\hat{S}_z + \gamma_e A_{yz}\hat{I}_y\hat{S}_z + \gamma_e A_{zz}\hat{I}_z\hat{S}_z - \omega_n\hat{I}_z, \tag{22}$$

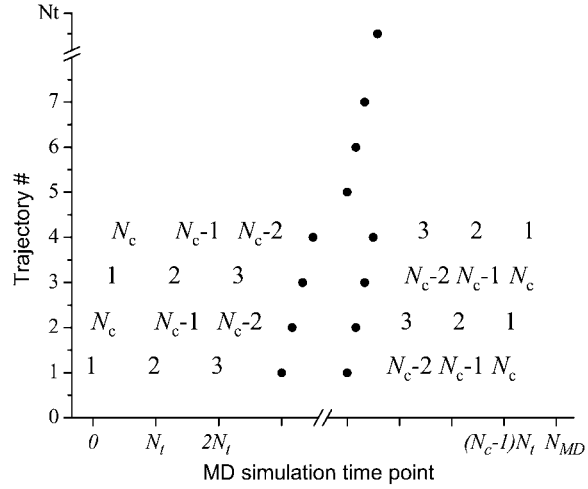

FIGURE 2 Diagram showing how N_t trajectories each consisting of N_c points are extracted from a single MD simulation consisting of N_{MD} points.

where β_e is the Bohr magneton, γ_e is the gyromagnetic ratio of the electron, H_0 is the direct-current magnetic field, ω_n is the nitrogen Larmor frequency, and ω_0 is the fixed microwave frequency. The appropriate elements of the g- and A-tensors are determined from

$$\hat{g} = \hat{R}(\Omega(t))\hat{g}_d\hat{R}^{-1}(\Omega(t)) \quad \hat{A} = \hat{R}(\Omega(t))\hat{A}_d\hat{R}^{-1}(\Omega(t)), \tag{23}$$

where g_d and A_d are the tensors diagonalized in the frame of the nitroxide. Analytical expressions for the eigenvalues and eigenvectors of this Hamiltonian have been derived with the aid of Mathematica 5.1 software (Wolfram Research, Champaign, IL). The eigenvalues, $\lambda_{m_S m_I}$ for $m_S = \alpha = +1/2$ or $m_S = \beta = -1/2$ and $m_I = 0$ or ± 1, are given by

$$\lambda_{m_S m_I} = m_S(g_{eff} + m_I\ell_{m_S}), \tag{24}$$

where

$$g_{eff} = \beta_e H_0 g_{zz} - \omega_0, \tag{25}$$

$$\ell_{m_S} = \sqrt{(\gamma_e A_{xz})^2 + (\gamma_e A_{yz})^2 + c_{m_S}^2}, \tag{26}$$

and

$$c_{m_S} = \gamma_e A_{zz} - 4m_S\omega_n. \tag{27}$$

The corresponding eigenvectors are given to within a normalization factor by Eqs. 28 using the basis set $\{\alpha + 1, \alpha\ 0, \alpha - 1, \beta + 1, \beta\ 0, \beta - 1\}$:

$$v_{m_S=\alpha\, m_I=\pm1} = \begin{pmatrix} \frac{(c_\alpha \pm \ell_\alpha)^2}{4b^2} \\ \frac{c_\alpha \pm \ell_\alpha}{\sqrt{2}b} \\ 1 \\ 0 \\ 0 \\ 0 \end{pmatrix} \quad v_{m_S=\alpha\, m_I=0} = \begin{pmatrix} \frac{-b^*}{b} \\ \frac{c_\alpha}{\sqrt{2}b} \\ 1 \\ 0 \\ 0 \\ 0 \end{pmatrix}$$

$$v_{m_S=\beta\, m_I=\pm1} = \begin{pmatrix} 0 \\ 0 \\ 0 \\ \frac{(c_\beta \pm \ell_\beta)^2}{4b^2} \\ \frac{c_\beta \pm \ell_\beta}{\sqrt{2}b} \\ 1 \end{pmatrix} \quad v_{m_S=\beta\, m_I=0} = \begin{pmatrix} 0 \\ 0 \\ 0 \\ \frac{-b^*}{b} \\ \frac{c_\beta}{\sqrt{2}b} \\ 1 \end{pmatrix}. \tag{28}$$

The FID is calculated by following the evolution of the spin density matrix, ρ, in the rotating frame as a function of time after a $\pi/2$ pulse. The density matrix at $t = 0$ is given by

$$\rho(t=0) = \begin{pmatrix} 0 & 0 & 0 & 1/3 & 0 & 0 \\ 0 & 0 & 0 & 0 & 1/3 & 0 \\ 0 & 0 & 0 & 0 & 0 & 1/3 \\ 1/3 & 0 & 0 & 0 & 0 & 0 \\ 0 & 1/3 & 0 & 0 & 0 & 0 \\ 0 & 0 & 1/3 & 0 & 0 & 0 \end{pmatrix}. \tag{29}$$

The time-dependent behavior of ρ is governed by the SLE:

$$\dot{\rho} = -i[H(\Omega(t)), \rho(t)]. \tag{30}$$

The solution to the SLE is given by

$$\rho(t+\tau) = \hat{Q}(t,\tau)\rho(t)\hat{Q}^{-1}(t,\tau) \tag{31}$$

and

$$\hat{Q}(t,\tau) = \hat{V}(t)\, e^{-i\Lambda(t)\tau}\, \hat{V}^{-1}(t), \tag{32}$$

where $\hat{V}(t)$ and $\Lambda(t)$ are the matrices of eigenvectors and eigenvalues of $\hat{H}(t)$, respectively. To account for additional relaxation effects, all of the elements of the 3×3 off-diagonal blocks of ρ are multiplied by

$$e^{-\tau/T_{2e}} \tag{33}$$

after each time increment of τ. In the rotating frame, the complex FID signal, $S_j(t)$, for a given trajectory j is given by

$$S_j(t) = Tr\{\hat{S}_+ \rho_j(t)\}. \tag{34}$$

Equation 34 gives the FID for a single trajectory. The ensemble-averaged FID is calculated by summing FIDs calculated from a large number of trajectories obtained by combining trajectories for the GRD of the protein with trajectories extracted from an MD simulation describing the internal dynamics of the protein and the local motions of the label. Trajectories for GRD start at randomly chosen values of the Euler angles defining the orientation of the protein in the laboratory frame. A program for implementing this approach was written in FORTRAN and run on a personal computer equipped with an Intel Pentium 4 processor.

A 100 G spectral width corresponds to a FID time increment of 3.6 ns. Thus the time increment, τ, required is on the order of nanoseconds. The FID of a nitroxide decays quickly (see below), thus most of the FID can be added by zero-padding to give the desired number of points. The number of points actually calculated using the equations above for each FID is given by N_c. The FID is then zero-padded to give a total of 2^{Np} points. CW-EPR spectra are obtained by fast Fourier transform of the complex FID followed by numerical calculation of the first derivative lineshape to mimic phase-sensitive detection of the Zeeman-modulated signal. Alternatively, modulation effects could be formulated as a mathematical filter (45).

SDSL of T4 lysozyme

Plasmids containing the genes for the single cysteine mutants T4L K65C and T4L F153C were kindly provided by Dr. Hassane Mchaourab (Vanderbilt University, Nashville, TN). T4L mutants were expressed and purified as previously described (46). Briefly, plasmids were transformed into competent *Escherichia coli* K38 cells. Isopropyl β-thiogalactoside (1 mM) was added to log phase cultures to induce protein expression for 90 min. The cell pellet was resuspended in a buffer containing 25 mM Tris, 25 mM MOPS and 0.2 mM EDTA (pH 7.6). The cells were then disrupted by sonication. After 30 min centrifugation at 10,000 $\times$ g, the supernatant was passed through a 0.2 μm filter. The flow through was then loaded on a Resource S cation-exchange column (Amersham Bioscience, Piscataway, NJ) and eluted with a NaCl gradient from 0 to 1 M. Protein concentration was determined by ultraviolet absorption at 280 nm using an extinction coefficient of 1.228 cm^2mg^{-1}. The purity of all T4L mutant proteins was at least 95%, as determined by SDS polyacrylamide gel electrophoresis. Single or double cysteine mutants were spin labeled with a 10- or 20-fold molar excess, respectively, of 1-oxyl-2,2,5,5-tetramethyl-Δ3-pyrroline-3-methyl methanethiosulfonate spin label (Toronto Research Chemicals, North York, Ontario, Canada) at room temperature for 10 min and then at 4°C overnight. Unreacted label was removed from all samples using a HiTrap desalting column (Amersham Bioscience, Piscataway, NJ) with desalting buffer containing 100 mM NaCl, 20 mM MOPS, 0.1 mM EDTA and 0.02% azide (pH 7.0). Proteins were then

concentrated in an Amicon Ultra-4 Centrifugal Filter Device (5000 nominal molecular weight limit, Millipore, Bedford, MA).

EPR spectroscopy

All EPR spectra were collected at X-band using a Bruker EMX spectrometer (BrukerBiospin, Billerica, MA) equipped with a TM_{110} cavity. All spectra were recorded at room temperature using 100 kHz Zeeman modulation of 1 G amplitude and a microwave power of 5 mW with samples contained in a 50 μL glass capillary tube. Measured spin label concentrations were $\sim$200 μM.

RESULTS

Timescale

Fig. 3 shows an experimental first-derivative EPR spectrum of T4L F153R1 (top panel), the integrated spectrum (*middle panel*, *shaded line*), and the first 200 ns of the FID given by the Fourier transform of the integrated spectrum (*bottom panel*). To test how long a time span is needed to simulate EPR spectra, the values of the FID were replaced by zero at times longer than 75 ns and the altered FID back-transformed to give the recovered spectrum (*middle panel*, *dashed solid line*). This recovered spectrum faithfully reproduces the original spectrum. On the other hand, setting the FID to zero at times longer than 25 ns resulted in a distorted spectrum (result not shown).

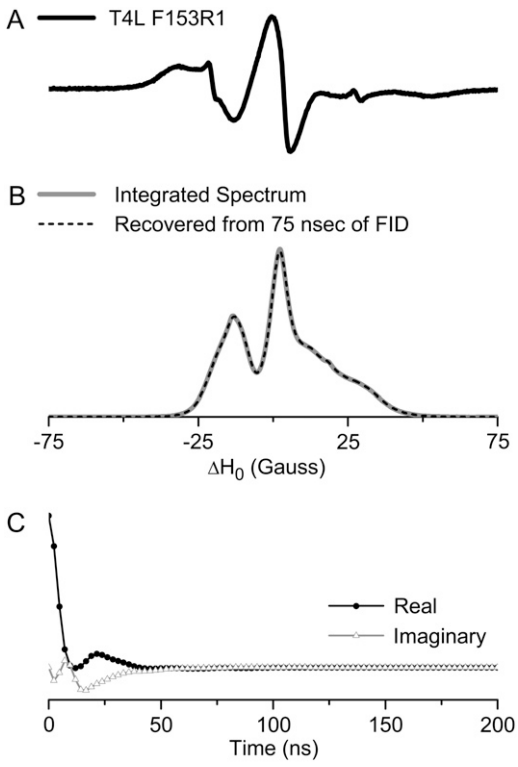

FIGURE 3 (*A*) Experimental room-temperature EPR spectrum of T4L F153R1 in buffer. (*B*) Integrated spectrum of T4L F153R1 *(solid shaded line*) and the spectrum recovered from back transform of the FID after zeroing values for time >75 ns (*dashed solid line*). (C) The first 200 ns of the real (*solid line*, *solid circles*) and imaginary (*shaded line*, *open triangles*) components of the Fourier transform (FID) of the integrated spectrum of T4L F153R1. The time increment is 2.38 ns per point.

Simulation of CW-EPR spectra for global rotational diffusion

Equations 1–16 describe a method for generating Brownian trajectories defining the orientation as a function of time of a spin label undergoing GRD. Equations 21–34 define an approach for simulating FIDs and the corresponding CW-EPR spectra from these trajectories. Fig. 4 shows calculated CW-EPR spectra (*solid shaded lines*) for isotropic, axially symmetric, and fully anisotropic rotational diffusion tensors. These spectra were calculated by setting all of the angles Ω_{MD} to zero ($\hat{R}_{MD} = \hat{1}$ and $\hat{R}_{PTD} = \hat{1}$) and using reasonable values of the nitroxide A- and g-tensors. The spectra calculated for isotropic and axially symmetric rotational diffusion are compared to spectra (*dashed solid lines*) calculated by finding the steady-state solution to the SLE using eigenfunction expansion as implemented by Robinson (22). Both sets of spectra are essentially identical. The simulations shown in Fig. 4, *A* and *B*, also agree with spectra calculated using the simulation program developed by Freed and coworkers (23) (data not shown). The results in Fig. 4 set the stage for using this same approach for calculated CW-EPR spectra directly from trajectories generated from MD simulations of spin-labeled proteins.

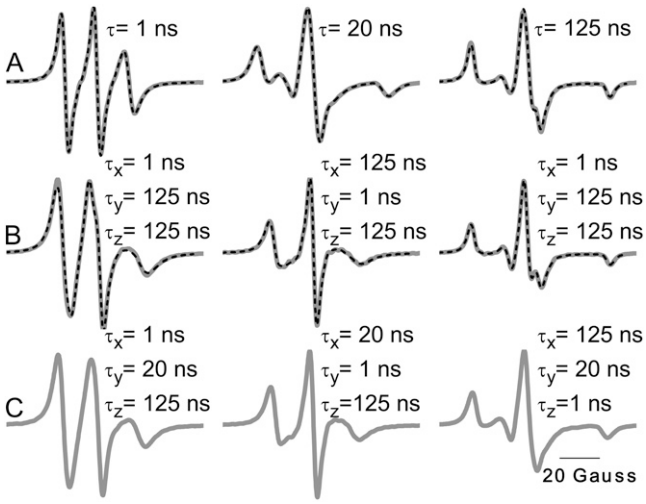

FIGURE 4 CW-EPR spectra (*solid shaded lines*) calculated from the first derivative of the Fourier transform of FIDs calculated from Brownian trajectories for (*A*) isotropic rotational diffusion, (*B*) axially symmetric rotational diffusion, and (*C*) fully anisotropic rotational diffusion. For all calculations the following tensor values were used: $g_{xx} = 2.0082$, $g_{yy} = 2.0060$, $g_{zz} = 2.0023$, $A_{xx} = 7.0$ G, $A_{yy} = 6.0$ G, and $A_{zz} = 36.0$ G. $T_{2e} = 28.4$ ns corresponding to an intrinsic linewidth of 2 G. Scan widths of 100 G are shown. FIDs were calculated from 50,000 trajectories ($N_t = 50{,}000$) with a time step of $\tau = 2$ ns out to 100 ns ($N_c = 50$) and then zero-padded to 2.046 μs ($N_p = 10$). For comparison, CW-EPR spectra calculated by the eigenfunction expansion approach (22) are shown (*dashed solid lines*) for isotropic and axially symmetric rotational diffusion.

MD simulations of the internal dynamics of spin-labeled T4L

MD simulations in explicit solvent were performed to define the dynamics of the protein backbone and spin-label tether for buried site T4L F153R1 and solvent-exposed site T4L K65R1 (see Fig. 1 *B*). The sites were chosen based on their extreme range of spin label mobility. The torsion angles χ_1, χ_2, χ_3, χ_4, and χ_5 of **R1** as a function of time for T4L F153R1 and T4L K65R1 are shown in Fig. 5. Initial values of the five torsion angles of **R1** for T4L F153R1 were chosen in an attempt to accommodate the spin-label side chain at the buried site. At ~410 ps of the MD simulation, there is an abrupt change in the orientation of the side chain due to changes in χ_2, χ_4, and χ_5. For the remainder of the MD simulation, the five torsion angles of the **R1** side chain of T4L F153R1 remain in one distinct rotameric state with mean values of $\chi_1 = -74°$ (**m**), $\chi_2 = -155°$ (**t**), $\chi_3 = -88°$, $\chi_4 = +149°$ (**t**), and $\chi_5 = -105°$ (**m**) (see Lovell et al. (47) for rotameric state nomenclature). Although a crystal structure of T4L K65R1 has been published by Hubbell and co-workers (48), the rotameric state of the **R1** side chain in their reported structure is heavily influenced by intermolecular contacts in the crystal lattice. Therefore, the initial values of the torsion angles of the spin-label side chain for T4L were chosen by analogy to other helix surface sites T4L 80, T4L 115, and T4L 119 (48,49). During the 75 ns MD simulation of T4L K65R1, there is considerable rotation about χ_4/χ_5 and to a lesser extent χ_1/χ_2. For both T4L F153R1 and T4L K65R1, χ_3 remains at $\sim -90°$ throughout the MD simulations. Fig. 6 shows polar plots of the histograms for the five torsion angles of T4L F153R1 and T4L K65R1.

The EPR spectrum of a spin label depends on the time-dependent changes in the Euler angles defining the orientation of the nitroxide with respect to the protein. These Euler angles for T4L F153R1 and T4L K65R1 are shown in Fig. 7.

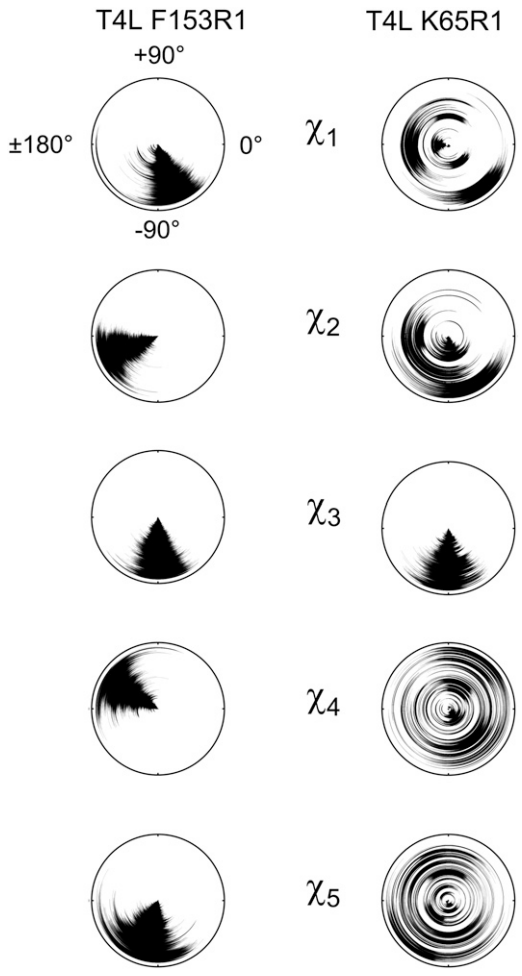

FIGURE 5 Values of the five torsion angles of **R1** defined in Fig. 1 *A* as a function of time from the 75 ns MD simulations of T4L F153R1 (*left*) and T4L K65R1 (*right*). Time increases along the radial axis, with $t = 0$ at the origin and $t = 75$ ns near the outer circumference.

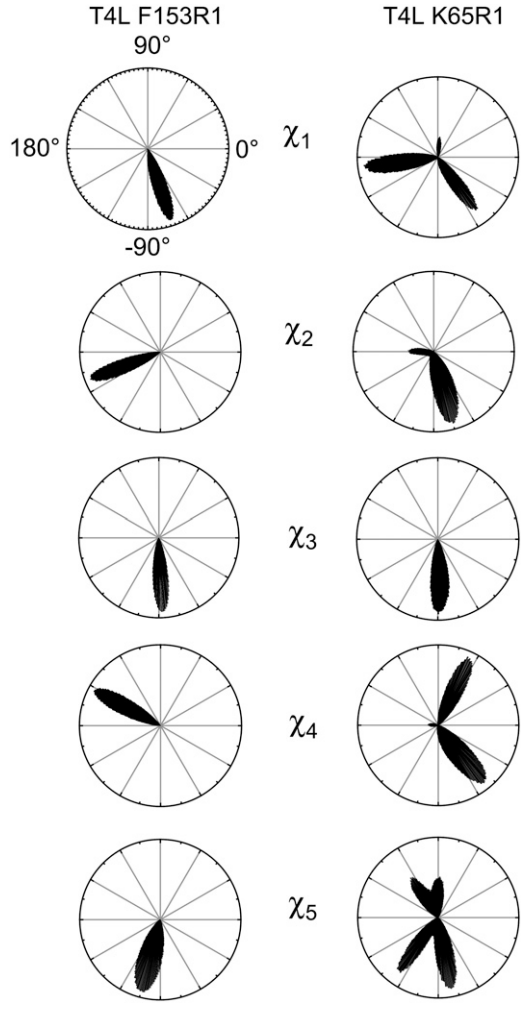

FIGURE 6 Histograms showing the distribution of the five torsion angles of **R1** from the 75 ns MD simulations of T4L F153R1 (*left*) and T4L K65R1 (*right*). Frequency counts of the various torsion angles were created with a bin width of 1° and plotted as polar bar graphs using Origin 7.5 software (OriginLab, Northampton, MA).

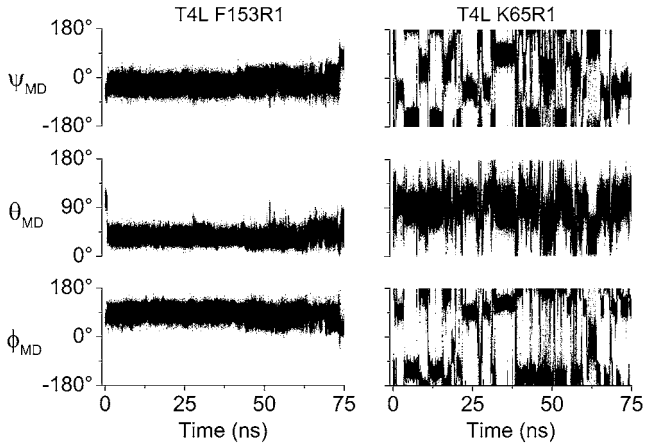

FIGURE 7 Values of the three Euler angles, Ω_{MD}, defining the orientation of the nitroxide with respect to a protein frame of reference from the MD simulations of T4L F153R1 (*left*) and T4L K65R1 (*right*).

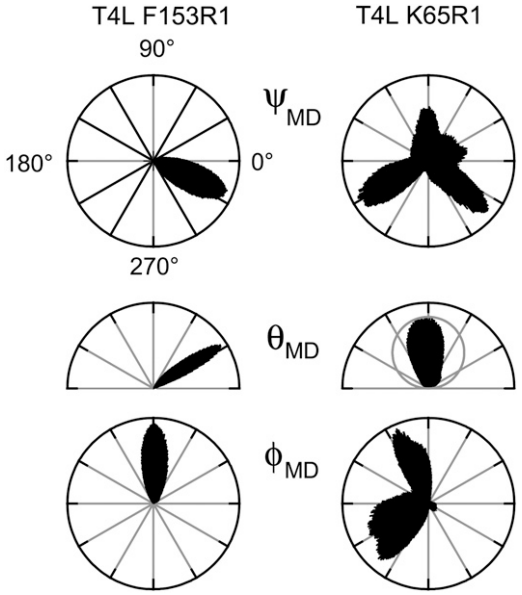

FIGURE 8 Histograms showing the distribution of the three Euler angles defining the orientation of the nitroxide with respect to a protein frame of reference from the 75 ns MD simulations of T4L F153R1 (*left*) and T4L K65R1 (*right*). Frequency counts of the Euler angles were created with a bin width of 1° and plotted as polar bar graphs using Origin 7.5 software (OriginLab). The shaded circle in the plot for θ_{MD} of T4L K65R1 corresponds to an isotropic distribution.

The time-dependent behavior of the Euler angles for T4L F153R1 and T4L K65R1 is consistent with both the behavior of the five torsion angles and with the expected behavior of a buried site and a helix-surface site. Given the change in χ_2, χ_4, and χ_5 observed for T4L F153R1 at ~410 ps, there is a corresponding change in the Euler angles for T4L F153R1. Given the abrupt change in the orientation of the nitroxide at ~410 ps, the first 1 ns of the MD simulations for both T4L F153R1 and T4L K65R1 were not used to calculate the corresponding CW-EPR spectra.

Histograms showing the distributions of the three Euler angles defining the orientation of the nitroxide with respect to the protein are shown in Fig. 8. All three Euler angles for T4L F153R1 are in narrow distributions, whereas the Euler angles for T4L K65R1 are more nearly isotropic. The distribution of the angle θ is characterized by a standard deviation of 10.5° for T4L F153R1 and 29.1° for T4L K65R1. For comparison an isotropic ($\sin\theta$-weighted) distribution of θ, which is shown as a shaded circle in Fig. 8, has a standard deviation of 39.1°.

Simulation of CW-EPR spectra for T4L F153R1 and T4L K65R1

Simulated and experimental CW-EPR spectra for T4L F153R1 and T4L K65R1 are shown in Fig. 9. Fig. 9 *A* shows a spectrum calculated assuming no internal or local dynamics for an isotropic rotational correlation time of $\tau_c = 6$ ns, which is the estimated rotational correlation time for T4L in aqueous buffer (1 cP) at room temperature (20°C) (49). The spectra in Fig. 9, *B* and *D*, were calculated with $\tau_c = 6$ ns combined with the local dynamics determined by trajectories extracted from the MD simulations of T4L F153R1 and T4L K65R1, respectively. The A- and g-tensors used for these simulations were taken from a fit to the CW-EPR spectrum of T4L K65R1 in high-viscosity solution at low temperature (50). Similar tensor values have been obtained from the combined analysis of 9-GHz and 250-GHz spectra of two spin-labeled sites in T4L (51). A 2 G line width ($T_{2e} = 28.4$ ns) gave a better match to the experimental data than either a 1 G or 4 G line width. The corresponding experimental spectra are shown in Fig. 9, *C* and *E*.

The calculated CW-EPR spectra in Fig. 9, *B* and *D*, demonstrate that the approach used in this work does provide sufficient sampling of the local dynamics of the nitroxide to give simulations that can be compared directly to experimental data. Moreover, the calculated spectra reasonably represent the experimental data. Comparing the spectrum calculated for $\tau_c = 6$ ns (Fig. 9 *A*) with that calculated for $\tau_c = 6$ ns combined with the local dynamics of T4L F153R1 (Fig. 9 *B*), it is apparent that the limited local dynamics of the label in a buried site have a modest effect on the simulation, which is consistent with the experimental data shown in Fig. 9 *C*. The increased dynamics calculated for the solvent-exposed T4L K65R1 result in a collapse of the simulated spectrum (Fig. 9 *D*) to nearly a simple three-line pattern consistent with the experimental data (Fig. 9 *E*).

DISCUSSION

The CW-EPR spectrum of a spin-labeled protein depends on the dynamics due to the overall Brownian tumbling of the protein, the internal motions of the protein, and the local motions of the probe. In this work, a quaternion-based Monte Carlo method has been used to generate Brownian trajecto-

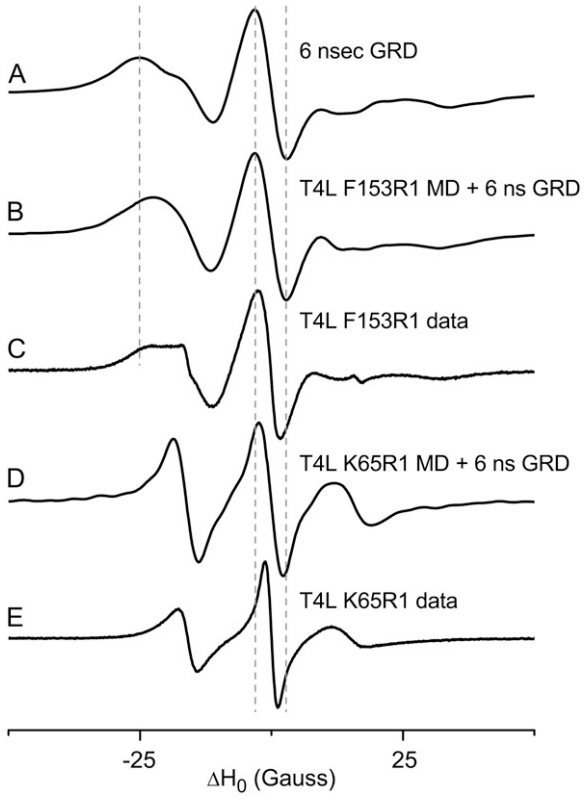

FIGURE 9 Calculated and experimental CW-EPR spectra of T4L F153R1 and T4L K65R1: (*A*) calculated spectrum corresponding to isotropic rotational diffusion with a correlation time of 6 ns; (*B*) calculated spectrum of T4L F153R1 showing the combined effects of GRD and plus the internal dynamics taken from the 75 ns MD simulation; (*C*) experimental room-temperature CW-EPR spectrum of T4L F153R1 in buffer; (*D*) calculated spectrum of T4L K65R1 showing the combined effects of GRD and plus the internal dynamics taken from the 75 ns MD simulation; and (*E*) experimental room-temperature CW-EPR spectrum of T4L K65R1 in buffer. For all calculations, $g_{xx} = 2.0082$, $g_{yy} = 2.0060$, $g_{zz} = 2.0023$, $A_{xx} = 6.4$ G, $A_{yy} = 5.5$ G, and $A_{zz} = 36.1$ G. T_{2e}= 28.4 ns; $N_c = 37$, $N_t = 10000$, and $N_p = 10$, $\tau = 2$ ns. Vertical dashed lines are included as an aid for comparing the spectra.

ries describing the global tumbling of the protein. MD simulations have been used to generate trajectories describing all of the internal and local dynamics. These trajectories are then combined and used to calculate ensemble-averaged FIDs from the time-dependent solution to the SLE. Fourier transforms of the FIDs give the desired CW-EPR spectra. This approach has been validated initially by calculating CW-EPR spectra for global tumbling alone (Fig. 4) and comparing them to spectra calculated using an eigenfunction expansion algorithm (22) to obtain a steady-state solution to the SLE. Results from eigenfunction expansion algorithms as developed independently by Freed and co-workers (23) and Robinson (22) provide a standard that has been used to validate the Monte Carlo approach developed here. The excellent agreement between simulated CW-EPR spectra calculated using the Monte Carlo algorithm and those calculated using an eigenfunction expansion algorithm for both isotropic rotational diffusion tensors (Fig. 4 *A*) and for axially symmetric rotational diffusion tensors (Fig. 4 *B*) demonstrate that the quaternion-based Monte Carlo approach provides a flexible, computationally efficient method for modeling rotational dynamics. The use of the quaternion-based algorithm for generating Brownian trajectories extends the previous work of Robinson and co-workers (19) so that spectra can be calculated for nitroxides with anisotropic A- and g-tensors undergoing fully anisotropic GRD (Fig. 4 *C*). Similar methods can be used to generate Brownian trajectories corresponding to other dynamic models. One intriguing possibility is the use of a Monte Carlo algorithm to explicitly model rotations about the five torsion angles of the **R1** side chain. Also, the methods developed here can be used to extend previous efforts to simulate the effects of dynamics on the CW-EPR spectra of pairs of dipolar-coupled nitroxides (52).

Eigenfunction expansion methods have been widely used to simulate CW-EPR spectra for more than three decades. These methods provide rapid calculations of lineshapes of nitroxides undergoing free rotational diffusion and motion in simple ordering potentials, which can be expressed analytically in terms of spherical harmonics. The alternative approach used in this work is suitable for those situations where the dynamics of the label are more complex. Thus, lineshapes can be calculated from dynamic trajectories obtained, for example, from a MD simulation without requiring the determination of an effective single-particle potential.

To estimate the time frame for which the calculated FID will have significant nonzero values, an experimental X-band CW-EPR spectrum was Fourier transformed. The results in Fig. 3 demonstrate that on the order of 75 ns of nonzero values are required to faithfully reproduce the corresponding CW-EPR spectrum. Given this time frame, it becomes practical to use MD simulations to model all of the internal and local dynamics of a spin-labeled protein. Fig. 2 shows a scheme that uses staggered initial times and alternating direction of time to generate multiple interleaved trajectories from a single MD simulation. Although these trajectories are not completely uncorrelated, this scheme has been developed in an effort to extract, from a single MD simulation, multiple trajectories that are sufficiently independent to calculate an ensemble-averaged CW-EPR spectrum.

Two sites were chosen for examination in this work to represent the wide range of site-dependent dynamics that are routinely observed in SDSL studies. As expected, during the MD simulation of T4L F153R1, the **R1** side chain, after an initial change in conformation within the first 1 ns, showed only small oscillations about a fixed rotameric state for all five torsion angles. The MD simulation of T4L K65R1 showed frequent changes in the rotameric states of χ_4/χ_5 and to a lesser extent χ_1/χ_2. The χ_4/χ_5 model predicts that the local motion of the **R1** side chain at helix surface sites is largely limited to oscillations about χ_4 and χ_5 (5,53). The MD simulation of T4L K65R1 shows multiple transitions between

rotameric states for both χ_1 and χ_2. Future work will address the question of whether the current MD simulation protocol overestimates the rotational mobility about χ_1 and χ_2.

MD simulations have been used in this work to model all of the local dynamics of the spin label. No additional parameters have been invoked to quantify the amplitude or rate of the local motions. The ability to calculate CW-EPR spectra directly from MD simulations provides a sensitive test of how accurately the MD simulations describe the site-specific dynamics of the **R1** side chain. Given the current state of the art for MD simulations, this approach may not be suitable for rapid, routine calculation of CW-EPR lineshapes. However, it does enable a detailed examination of how well MD simulates the dynamics of the spin label in a variety of different labeling topographies with the goal of evaluating the parameterization of **R1**. Additional sites have been identified, including tertiary contact, helix N-terminal, helix C-terminal, and loop sites, which are the subject of ongoing examination.

The dynamics of the **R1** side chain plays a fundamental role in determining the lineshape obtained in SDSL studies. Similarly, the disorder of **R1** plays a fundamental role in low temperature nitroxide-nitroxide distance measurements by both CW-EPR and pulsed EPR. A detailed, context-specific understanding of **R1** disorder is important to the analysis of these distance measurements, and a number of laboratories are developing approaches to model the **R1** side chain. Accurate modeling of the dynamics of single **R1** side chains in spin-labeled proteins at ambient temperatures can provide important constraints to the development of models for the disorder of pairs of labels at low temperatures.

The global tumbling of T4L was modeled as isotropic rotational diffusion with a correlation time of 6 ns. No attempt has been made to optimize this number in this work, nor has any attempt been made to consider anisotropic global rotational diffusion models. Nevertheless, it is apparent from the simulation in Fig. 9 *A* that an isotropic $\tau_c = 6$ ns underestimates the total dynamics of the nitroxide for both T4L F153R1 and T4L K65R1. Including the local dynamics calculated for T4L F153R1 results in a slight narrowing of the high and low field *z*-turning points of the simulation (Fig. 9 *B*), which is consistent with the experimental spectrum (Fig. 9 *C*). The simulation for T4L K65R1 (Fig. 9 *D*) is a motionally narrowed spectrum that is also consistent with the experimental spectrum (Fig. 9 *E*). The ratio of the peak heights for the T4L K65R1 simulation does not, however, match those of the experimental data. In fact, the center manifold of the simulated spectra at both sites is noticeably broader than that of the experimental data. One possible explanation for this discrepancy is that the use of an isotropic $\tau_c = 6$ ns may not be adequate to properly model the global tumbling of T4L. The simulation of experimental CW-EPR spectra may be improved by taking advantage of a method for estimating the rotational diffusion tensor of a protein of known structure, which has been developed by Aragon (54). Secondly, the MD simulation may somewhat overestimate the local dynamics at the helix surface site T4L K65R1, particularly about χ_1 and χ_2. The combination of MD simulations, the corresponding simulated CW-EPR spectra, and the associated CW-EPR data from other sites on T4L will continue to be used to further test how well MD defines the internal and local dynamics of a spin-labeled protein. Finally, the Hamiltonian (Eq. 22) does not include nonsecular ($\widehat{S}_{\pm}$) terms. Thus, the relaxation processes resulting from stochastic modulation of these terms are not included in the current calculations. An attempt has been made to account for these relaxation processes by including a post hoc relaxation term (Eq. 33). Additional theory is being developed to rigorously include the nonsecular terms in the spin Hamiltonian to test for any significant lineshape effects from these additional terms.

All of the above factors may play a role in any apparent discrepancy between simulation and experiment in Fig. 9. To resolve these issues, it may also prove very useful to use high field (HF) CW-EPR. At higher fields, CW-EPR spectra are less sensitive to the global tumbling of the protein and more sensitive to the rapid local motions than at X-band (17,51,55). Given the increased breadth of a HF CW-EPR spectrum, the corresponding HF FID will decay to zero more quickly than at X-band. On the other hand, given the increased dependence of the resonance condition on orientation at high field, simulation of HF CW-EPR requires increased sampling. How these two factors play against each other is the subject of ongoing research. Preliminary results suggest that the approach developed in this work can be readily adapted to the simulation of high field spectra.

Two component spectra are commonly observed in SDSL studies using MTSSL (46,56). The two components can be assigned to two conformational states of the MTSSL side chain with differing degrees of mobility (48,49,55,57). Given that the two components are resolved in CW-EPR spectra, interconversion between the two conformational states must be slow or nonexistent on the CW-EPR timescale. Thus, it cannot be expected that a single MD simulation spanning 50–100 ns will capture all of the relevant conformational states for all labeling sites. The accelerated MD method proposed recently by Hamelberg and co-workers offers a particularly appealing strategy to enhance dramatically the protein conformational sampling in these calculations, using the current computational protocols and potential function models (58,59).

SUMMARY

CW-EPR spectra of spin-labeled proteins have been simulated using a combination of a quaternion-based Monte Carlo algorithm to model the global tumbling of the protein together with MD simulations to model the internal dynamics of the protein and the local dynamics of the label side chain. Simulated spectra have been obtained, which are in reasonable agreement with X-band CW-EPR data from both a

motionally restricted buried site and a mobile helix surface site on T4 lysozyme. A foundation has been laid for exploring the agreement between theory and experiment for other labeling sites, for adapting this approach to other dynamic models, for extending this work to include additional terms in the spin Hamiltonian (notably dipolar coupling between labels), and for simulating data from high-field EPR experiments.

Dr. Bruce H. Robinson and Bruce E. Eichinger provided valuable insight into the generation of Brownian trajectories using quaternions. The authors also thank Dr. Robinson for critiquing the manuscript before submission. Suzanne Brandon prepared the T4L samples.

This work was supported by National Institutes of Health (NIH) EB002040, NIH HL34737, and NIH GM081661. D.P.R. was supported by NIH GM65944. S.C.D. was supported by a Vanderbilt University Discovery Grant.

REFERENCES

1. Hubbell, W. L., and C. Altenbach. 1994. Investigation of structure and dynamics in membrane proteins using site-directed spin-labeling. *Curr. Opin. Struct. Biol.* 4:566–573.
2. Hustedt, E. J., and A. H. Beth. 1999. Nitroxide spin-spin interactions: applications to protein structure and dynamics. *Annu. Rev. Biophys. Biomol. Struct.* 28:129–153.
3. Mchaourab, H. S., and E. Perozo. 2000. Determination of protein folds and conformational dynamics using spin-labeling EPR spectroscopy. *In* Biological Magnetic Resonance. L. J. Berliner, G. R. Eaton, and S. S. Eaton, editors. Kluwer Academic/Plenum Publishers, New York. 614.
4. Hubbell, W. L., D. S. Cafiso, and C. Altenbach. 2000. Identifying conformational changes with site-directed spin labeling. *Nat. Struct. Biol.* 7:735–739.
5. Columbus, L., and W. L. Hubbell. 2002. A new spin on protein dynamics. *Trends Biochem. Sci.* 27:288–295.
6. Klug, C. S., and J. B. Feix. 2005. SDSL: A survey of biological applications. *In* Biological Magnetic Resonance. S. S. Eaton, G. R. Eaton, and L. J. Berliner, editors. Kluwer Academic/Plenum Publishers, New York, NY. 269–308.
7. Fanucci, G. E., and D. S. Cafiso. 2006. Recent advances and applications of site-directed spin labeling. *Curr. Opin. Struct. Biol.* 16:644–653.
8. Steinhoff, H.-J., and W. L. Hubbell. 1996. Calculation of electron paramagnetic resonance spectra from Brownian dynamics trajectories: application to nitroxide side chains in proteins. *Biophys. J.* 71:2201–2212.
9. Steinhoff, H.-J., M. Muller, C. Beier, and M. Pfeiffer. 2000. Molecular dynamics simulation and EPR spectroscopy of nitroxide side chains in bacteriorhodopsin. *J. Mol. Liq.* 84:17–27.
10. Constantine, K. L. 2001. Evaluation of site-directed spin labeling for characterizing protein-ligand complexes using simulated restraints. *Biophys. J.* 81:1275–1284.
11. LaConte, L. E. W., V. Voelz, W. Nelson, M. Enz, and D. D. Thomas. 2002. Molecular dynamics simulation of site-directed spin labeling: experimental validation in muscle fibers. *Biophys. J.* 83:1854–1866.
12. Sale, K., C. Sar, K. A. Sharp, K. Hideg, and P. G. Fajer. 2002. Structural determination of spin label immobilization and orientation: a Monte Carlo minimization approach. *J. Magn. Reson.* 156:104–112.
13. Stoica, I. 2004. Using molecular dynamics to simulate electron spin resonance spectra of T4 lysozyme. *J. Phys. Chem. B.* 108:1771–1782.
14. Sale, K., L. K. Song, Y. S. Liu, E. Perozo, and P. Fajer. 2005. Explicit treatment of spin labels in modeling of distance constraints from dipolar EPR and DEER. *J. Am. Chem. Soc.* 127:9334–9335.
15. Borovykh, I. V., S. Ceola, P. Gajula, P. Gast, H. J. Steinhoff, and M. Huber. 2006. Distance between a native cofactor and a spin label in the reaction centre of *Rhodobacter sphaeroides* by a two-frequency pulsed electron paramagnetic resonance method and molecular dynamics simulations. *J. Magn. Reson.* 180:178–185.
16. Beier, C., and H. J. Steinhoff. 2006. A structure-based simulation approach for electron paramagnetic resonance spectra using molecular and stochastic dynamics simulations. *Biophys. J.* 91:2647–2664.
17. Budil, D. E., K. L. Sale, K. A. Khairy, and P. G. Fajer. 2006. Calculating slow-motional electron paramagnetic resonance spectra from molecular dynamics using a diffusion operator approach. *J. Phys. Chem. A.* 110:3703–3713.
18. Murzyn, K., T. Rog, W. Blicharski, M. Dutka, J. Pyka, S. Szytula, and W. Froncisz. 2006. Influence of the disulfide bond configuration on the dynamics of the spin label attached to cytochrome *C*. *Proteins.* 62: 1088–1100.
19. Robinson, B. H., L. J. Slutsky, and F. P. Auteri. 1992. Direct simulation of continuous wave electron paramagnetic resonance spectra from Brownian dynamics trajectories. *J. Chem. Phys.* 97:2609–2616.
20. Eviatar, H., U. A. Vanderheide, and Y. K. Levine. 1995. Computer simulations of the electron spin resonance spectra of steroid and fatty acid nitroxide probes in bilayer systems. *J. Chem. Phys.* 102:3135–3145.
21. Håkansson, P., P.-O. Westlund, E. Lindahl, and O. Edholm. 2001. A direct simulation of EPR slow-motion spectra of spin labelled phospholipids in liquid crystalline bilayers based on a molecular dynamics simulation of the lipid dynamics. *Phys. Chem. Chem. Phys.* 3:5311–5319.
22. Robinson, B. H. 1983. Effects of overmodulation on saturation transfer EPR signals. *J. Chem. Phys.* 72:1312–1324.
23. Schneider, D. J., and J. H. Freed. 1989. Calculating slow motional magnetic resonance spectra: a user's guide. *In* Biological Magnetic Resonance. L. J. Berliner, and J. Reuben, editors. Plenum Press, New York. 1–76.
24. DeSensi, S. C., D. Rangel, T. P. Lybrand, and E. J. Hustedt. 2007. The calculation of nitroxide CW-EPR spectra from Brownian dynamic trajectories and molecular dynamics simulation. 2007 Biophysical Society Meeting Abstracts. *Biophys. J.* Supplement, 339A.
25. Matubayasi, N., and M. Nakahara. 1999. Reversible molecular dynamics for rigid bodies and hybrid Monte Carlo. *J. Chem. Phys.* 110: 3291–3301.
26. Karney, C. F. F. 2007. Quaternions in molecular modeling. *J. Mol. Graph. Model.* 25:595–604.
27. Fedchenia, I. I., P. O. Westlund, and U. Cegrell. 1993. Brownian dynamic simulation of restricted molecular diffusion. The symmetrical and deformed cone models. *Mol. Simul.* 11:373–393.
28. Edmonds, A. R. 1974. Angular Momentum in Quantum Mechanics, 2nd edition. Princeton University Press, Princeton, NJ.
29. Gebe, J. A., J. J. Delrow, P. J. Heath, B. S. Fujimoto, D. W. Stewart, and J. M. Schurr. 1996. Effects of Na+ and Mg2+ on the structures of supercoiled DNAs: comparison of simulations with experiments. *J. Mol. Biol.* 262:105–128.
30. Frisch, M. J., G. W. Trucks, H. B. Schlegel, G. E. Scuseria, M. A. Robb, J. R. Cheeseman, V. G. Zakrzewski, J. A. Montgomery, R. E. Stratmann, J. C. Burant, S. Dapprich, J. M. Millam, A. D. Daniels, K. N. Kudin, M. C. Strain, O. Farkas, J. Tomasi, V. Barone, M. Cossi, R. Cammi, B. Mennucci, C. Pomelli, C. Adamo, S. Clifford, J. Ochterski, G. A. Petersson, P. Y. Ayala, Q. Cui, K. Morokuma, D. K. Malick, A. D. Rabuck, K. Raghavachari, J. B. Foresman, J. Cioslowski, J. V. Ortiz, B. B. Stefanov, G. Liu, A. Liashenko, P. Piskorz, I. Komaromi, R. Gomperts, R. L. Martin, D. J. Fox, T. Keith, M. A. Al-Laham, C. Y. Peng, A. Nanayakkara, C. Gonzalez, M. Challacombe, P. M. W. Gill, B. G. Johnson, W. Chen, M. W. Wong, J. L. Andres, M. Head-Gordon, E. S. Replogle, and J. A. Pople. 1998. Gaussian 98. Pittsburgh, PA.
31. Lajzerowicz-Bonneteau, J. 1976. Molecular structures of nitroxides. *In* Spin Labeling Theory and Applications. L. J. Berliner, editor. Academic Press, New York. 239–272.

32. Cornell, W. D., P. Cieplak, C. I. Bayly, I. R. Gould, K. M. Merz, D. M. Ferguson, D. C. Spellmeyer, T. Fox, J. W. Caldwell, and P. A. Kollman. 1995. A second generation force-field for the simulation of proteins, nucleic-acids, and organic molecules. *J. Am. Chem. Soc.* 117:5179–5197.

33. Cornell, W. D., P. Cieplak, C. I. Bayly, I. R. Gould, K. M. Merz, D. M. Ferguson, D. C. Spellmeyer, T. Fox, J. W. Caldwell, and P. A. Kollman. 1995. A second generation force field for the simulation of proteins, nucleic acids, and organic molecules. *J. Am. Chem. Soc.* 117:5179–5197.

34. Barone, V., A. Bencini, M. Cossi, A. Di Matteo, M. Mattesini, and F. Totti. 1998. Assessment of a combined QM/MM approach for the study of large nitroxide systems in vacuo and in condensed phases. *J. Am. Chem. Soc.* 120:7069–7078.

35. Wang, J. M., P. Cieplak, and P. A. Kollman. 2000. How well does a restrained electrostatic potential (RESP) model perform in calculating conformational energies of organic and biological molecules? *J. Comput. Chem.* 21:1049–1074.

36. Case, D. A., T. A. Darden, T. E. Cheatham 3rd, C. L. Simmerling, J. Wang, R. E. Duke, R. Luo, K. M. Merz, B. Wang, D. A. Pearlman, M. Crowley, S. Brozell, V. Tsui, H. Gohlke, J. Mongan, V. Hornak, G. Cui, P. Beroza, C. Schafmeister, J. W. Caldwell, W. S. Ross, and P. A. Kollman. 2004. AMBER 8. University of California, San Francisco.

37. Matsumura, M., J. A. Wozniak, S. Dao-pin, and B. W. Matthews. 1989. Structural studies of mutants of T4 lysozyme that alter hydrophobic stabilization. *J. Biol. Chem.* 264:16059–16066.

38. Swanson, E. 1995. PSSHOW. University of Washington, Seattle, WA.

39. Berendsen, H. J. C., J. R. Grigera, and T. P. Straatsma. 1987. The missing term in effective pair potentials. *J. Phys. Chem.* 91:6269–6271.

40. Darden, T., D. York, and L. Pedersen. 1993. Particle mesh Ewald—an N.Log(N) method for Ewald sums in large systems. *J. Chem. Phys.* 98:10089–10092.

41. Ryckaert, J. P., G. Ciccotti, and H. J. C. Berendsen. 1977. Numerical-integration of Cartesian equations of motion of a system with constraints—molecular-dynamics of N-alkanes. *J. Comput. Phys.* 23:327–341.

42. Price, D. J., and C. L. Brooks. 2004. A modified TIP3P water potential for simulation with Ewald summation. *J. Chem. Phys.* 121:10096–10103.

43. Arbuckle, B. W., and P. Clancy. 2002. Effects of the Ewald sum on the free energy of the extended simple point charge model for water. *J. Chem. Phys.* 116:5090–5098.

44. Moth, C. W., J. E. J. Prusakiewicz, L. J. Marnett, and T. P. Lybrand. 2005. Stereoselective binding of indomethacin ethanolamide derivatives to cyclooxygenase-1. *J. Med. Chem.* 48:3613–3620.

45. Nielsen, R. D., E. J. Hustedt, A. H. Beth, and B. H. Robinson. 2004. Formulation of Zeeman modulation as a signal filter. *J. Magn. Reson.* 170:345–371.

46. Mchaourab, H. S., M. A. Lietzow, K. Hideg, and W. L. Hubbell. 1996. Motion of spin-labeled side chains in T4 lysozyme. Correlation with protein structure and dynamics. *Biochemistry.* 35:7692–7704.

47. Lovell, S. C., J. M. Word, J. S. Richardson, and D. C. Richardson. 2000. The penultimate rotamer library. *Proteins.* 40:389–408.

48. Langen, R., K. J. Oh, D. Cascio, and W. L. Hubbell. 2000. Crystal structures of spin labeled T4 lysozyme mutants: Implications for the interpretation of EPR spectra in terms of structure. *Biochemistry.* 39: 8396–8405.

49. Guo, Z., D. Cascio, K. Hideg, T. Kalai, and W. L. Hubbell. 2007. Structural determinants of nitroxide motion in spin-labeled proteins: Tertiary contact and solvent-inaccessible sites in helix G of T4 lysozyme. *Protein Sci.* 16:1069–1086.

50. Hustedt, E. J., R. A. Stein, L. Sethaphong, S. Brandon, Z. Zhou, and S. C. DeSensi. 2006. Dipolar coupling between nitroxide spin labels: the development and application of a tether-in-a-cone model. *Biophys. J.* 90:340–356.

51. Barnes, J. P., Z. C. Liang, H. S. McHaourab, J. H. Freed, and W. L. Hubbell. 1999. A multifrequency electron spin resonance study of T4 lysozyme dynamics. *Biophys. J.* 76:3298–3306.

52. Hustedt, E. J., A. I. Smirnov, C. F. Laub, C. E. Cobb, and A. H. Beth. 1997. Molecular distances from dipolar coupled spin-labels: the global analysis of multifrequency continuous wave electron paramagnetic resonance data. *Biophys. J.* 72:1861–1877.

53. Columbus, L., T. Kálai, J. Jekö, K. Hideg, and W. L. Hubbell. 2001. Molecular motion of spin labeled side chains in alpha-helices: Analysis by variation of side chain structure. *Biochemistry.* 40:3828–3846.

54. Aragon, S., and D. K. Hahn. 2006. Precise boundary element computation of protein transport properties: diffusion tensors, specific volume, and hydration. *Biophys. J.* 91:1591–1603.

55. Liang, Z. C., Y. Lou, J. H. Freed, L. Columbus, and W. L. Hubbell. 2004. A multifrequency electron spin resonance study of T4 lysozyme dynamics using the slowly relaxing local structure model. *J. Phys. Chem. B.* 108:17649–17659.

56. McHaourab, H. S., T. Kalai, K. Hideg, and W. L. Hubbell. 1999. Motion of spin-labeled side chains in T4 lysozyme: Effect of side chain structure. *Biochemistry.* 38:2947–2955.

57. Tombolato, F., A. Ferrarini, and J. H. Freed. 2006. Modeling the effects of structure and dynamics of the nitroxide side chain on the ESR spectra of spin-labeled proteins. *J. Phys. Chem. B.* 110:26260–26271.

58. Hamelberg, D., C. A. F. de Oliveira, and J. A. McCammon. 2007. Sampling of slow diffusive conformational transitions with accelerated molecular dynamics. *J. Chem. Phys.* 127:155102-1–155102-9.

59. Hamelberg, D., J. Mongan, and J. A. McCammon. 2004. Accelerated molecular dynamics: A promising and efficient simulation method for biomolecules. *J. Chem. Phys.* 120:11919–11929.